range bias estimation. In addition to the segment or arc-specific parameters, the solution for parameters common to most arcs includes the Love number, rotation parameters, Mars satellite parameters, the mean spherical harmonic gravity field to degree 85, and seasonal J_2 and J_3 as

$$\delta J_n = \sum_{j=1}^{4} (C_j^n \cos j\ell' + S_j^n \sin j\ell').$$

9. Starting from an orientation model of Mars similar to that of Folkner *et al*. (*2*), the rotational parameters we estimate are the epoch obliquity (ε) and longitude of the Mars pole (ψ), the precession rate of the pole ($d\psi/dt$), the obliquity rate ($d\varepsilon/dt$), the rotation rate ($d\phi/dt$), and the seasonal variations in rotation angle as a periodic series

$$\delta\phi = \sum_{j=1}^{4} (C_j \cos j\ell' + S_j \sin j\ell')$$

where ℓ' is the Mars mean anomaly. The rigid-body nutation model is fixed to that of (*10*).
10. R. D. Reasenberg *et al*., *J. Geophys. Res*. **82**, 369 (1977).
11. A. S. Konopliv *et al*., *Geophy. Res. Lett*. **23**, 1857 (1996).
12. The drag model uses six flat plates to represent the spacecraft bus, antenna, and solar arrays with orientation provided by spacecraft telemetry. The atmospheric density is given by the Mars GRAM 3.4 model in C. J. Justus, D. L. Johnson, B. F. James, *NASA Tech. Memo. No. 108513* (1996). We also tested solving for a drag coefficient only once per day, and this did not change the results.
13. The orbit inclination is chosen such that $d\Omega/dt = -3/2\cos I J_2 (R/a')^2 n = n'$. Also, the MGS orbit elements are: a = 3796 km, e = 0.0084, period = 1.96 hours, and I = 92.9°.
14. The nutations of Mars pole ($\delta\varepsilon$ and $\delta\psi$) result in the following changes in orbit inclination relative to a space-fixed reference frame (*15*, *22*):

$$\frac{dI_{nut}}{dt} \cong -n'[\delta\varepsilon\cos\varepsilon\sin(\Omega-\psi) - \delta\psi\sin\varepsilon\cos(\Omega-\psi)]$$

The principal annual term for rigid-body response is $\delta\varepsilon = 0.0$ and $\varepsilon\delta\psi = -0.259''\sin\ell'$. This reduces the secular rate by about 10%. The fluid core can further reduce rate by up to 1%.
15. C. F. Yoder, *Icarus* **117**, 250 (1995).
16. A phase lag ($= 1/Q$) can be introduced in the angle arguments in Eq. 2 in order to account for solid friction. For example $2(\Omega - L')$ is replaced with $2(\Omega - L') - 1/Q$. This effect reduces the observed signature by about 1%.
17. The inclination drift does cause a secular acceleration in the node ($d\Omega_{\delta I}/dt \cong -n'\tan\delta I$) that has about the same amplitude as the secular change in inclination after ~20 days. Thus, both node and inclination drift contribute to the global Love number solution. However, space craft maneuvers aimed at desaturation of the momentum wheels and maintaining orbit geometry may limit the sensitivity to long-term orbit changes.
18. $d\Omega_{k_{22}}/dt \cong k_{22} n' T\cos I[\cos^4(\varepsilon/2)\cos 2(\Omega - L') + {}^1/_2\sin^2(\varepsilon/2)\cos 2(\Omega - \psi)]$, $dI_{k_{21}}/dt \cong k_{21} n' T\cos I\sin\varepsilon[\cos\varepsilon\sin(\Omega - \psi) + {}^1/_2\cos^2(\varepsilon/2)\sin(\Omega + \psi - 2L')]$
19. Let $\Omega = L' + \theta$. It happens that $L' - \psi \approx 260°$ during face-on (August 1999 and June 2001). We find $[\cos\varepsilon\cos(\Omega - \psi) + 1/2\cos^2(\varepsilon/2)\cos(\Omega + \psi - L')] = 0$ for $\sin\theta \approx 0.5$, corresponding to 2:00 p.m. local Mars time.
20. C. F. Yoder *et al*., *Nature* **303**, 757 (1983).
21. The scalar factors $f_n(x)$ are $x = \sin^2 I$, $f_4 = 5/8(R/a)^2(7x - 4)$, and $f_6 = -5/8(R/a)^4[7 - 54x + (62 + 5/8)x^2]$. The effect of odd J_n on spacecraft orbit e and argument of pericenter ω is obtained from the equation $dp/dt + iw_o p = 3/2 n\sin I(R/a)^3 f_3 \delta J_{odd}$

$$\delta J_{odd} = \sum_{j=1} (f_{2j+1}/f_3)\delta J_{2j+1}$$

The variable $p = e\exp(-i\omega)$ while $i = \sqrt{-1}$, $w_o \cong 3n(R/a)^2 f_3$, and the scalars are $f_3 = (1 - 5/4x)$, $f_5 = -5/16(R/a)^2(8 - 28x + 21x^2)$, and $f_7 = 35/64(R/a)^4[8 - 54x + 99x^2 - (53 + 5/8)x^3]$. Also, the mean orbit eccentricity $e \approx (R/a)(J_3/J_2)$ is due primarily to this forcing.
22. C. F. Yoder *et al*., *J. Geophys. Res*. **102**, 4065 (1997).
23. Solutions for k_{21} range from −0.1 to 0.1.
24. The latest estimate for (unnormalized) J_2 is $1.985683(3) \times 10^{-3}$ (Mars R_e = 3394.2 km), and the precession rate is [see (*2*, *10*, *22*)] $d\psi/dt = [-7606(0.365 M R_e^2/C) \times 10^{-3}$ arc sec/year $+ d\psi/dt_p + d\psi/dt_g]$, where the contribution from Jupiter is $d\psi/dt_p = -0.2 \times 10^{-3}$ arc sec/year and geodetic precession is $d\psi/dt_g = +6.7 \times 10^{-3}$ arc sec/year.
25. In the estimation process, the Doppler data are treated as uncorrelated measurements, i.e., white noise. Solar plasma, troposphere, and ionosphere can cause correlations in the measurements that are impractical to account for in a least-squares estimation process.
26. R. M. Haberle *et al*., *J. Geophys. Res. (Planets)* **104**, 8957 (1999).
27. The semidiurnal surface pressure field due to solar heating can be approximated by $\delta P_{22}|\sin\vartheta|^3\cos(2\alpha + 41°)$, where δP_{22} is the equatorial amplitude (Pathfinder pressure data indicate $\delta P_{22} \cong 0.011 P_0$). The global mean pressure $P_0 \cong 5.6$ mbar, and the hour angle $\alpha = 0$ at midnight (see SOM Text for more details). However, the estimate from one GCM (*29*) has the same phase, but ½ the amplitude. The atmospheric $k_2^a \cong 3.08(1 + k_2')R^2/gM_{sun}(R/a')^3\delta P_{22}\sin 2(\Omega - L' + 41°)/\sin 2(\Omega - L')$. Surface gravity g = 0.372 m/s² and the load $k_2' \cong -0.8k_2$. Thus, $k_2^a \approx 0.008$.
28. E. Groten *et al*., *Astron. J*. **111**, 1388 (1996).
29. F. Sohl, T. Spohn, *J. Geophys. Res*. **102**, 1613 (1997).
30. V. N. Zharkov, Gudkova, *Phys. Earth Planet. Inter*. **117**, 407 (2000).
31. C. F. Yoder, in A *Handbook of Physical Constants: Global Earth Physics* (AGU, Washington, DC, 1995), vol. 1, pp. 1–31.
32. R. D. Ray *et al*., *Nature* **381**, 585 (1996).
33. Compressed mean core density at core temperature ranges from 5.2 g/cm³ [high pressure Fe(0.9)S (and $\chi_c = 1$)] to 7.5 g/cm³ ($\chi_c = 0$), and this poses limits on core size represented by the upper and lower bounds on core radius shown in model calculations in Fig. 2.
34. J. O. Dickey *et al*., *Science* **265**, 482 (1994).
35. A. S. Konopliv *et al*., *Icarus* **150**, 1 (2001).
36. The most recent lunar Love number from Lunar Prospector (*35*) is $k_2 = 0.025 \pm 0.003$. The model estimate (*34*) is $k_2 = 0.022$ without partial melt at depth.
37. The mass change in the southern cap ranges from 5.7×10^{15} (model C) to 11.3×10^{15} kg (model A). The corresponding density (*5*) is 1900 to 3800 kg/m³. This suggests that at least the south cap volume is larger than reported.
38. The ratio J_5/J_3 is 0.224 (model A), 0.436 (model B), and 0.561 (model C). The ratio f_5/f_3 is 0.97 for MGS (*21*) (table S1).
39. D. E. Smith *et al*., *J. Geophys. Res*. **104**, 1885 (1999).
40. E. Van den Acker *et al*., *J. Geophys. Res. (Planets)* **105**, 24563 (2000).
41. We thank J. G. Williams, C. K. Shum, and V. Dehant for thoughtful reviews and J. T. Schofield for advice and Pathfinder pressure data. The research described in this paper was carried out by the Jet Propulsion Laboratory, California Institute of Technology, under a contract with NASA.

Supporting Online Material
www.sciencemag.org/cgi/content/full/1079645/DC1
SOM Text
Figs. S1 to S6
Tables S1 to S3

22 October 2002; accepted 19 February 2003
Published online 6 March 2003;
10.1126/science.1079645
Include this information when citing this paper.

REPORTS

Band Structure and Fermi Surface of Electron-Doped C_{60} Monolayers

W. L. Yang,[1,3] V. Brouet,[3,1,4] X. J. Zhou,[3] Hyoung J. Choi,[5] Steven G. Louie,[2,5] Marvin L. Cohen,[2,5] S. A. Kellar,[3] P. V. Bogdanov,[3] A. Lanzara,[3] A. Goldoni,[6] F. Parmigiani,[7] Z. Hussain,[1] Z.-X. Shen[3]*

C_{60} fullerides are challenging systems because both the electron-phonon and electron-electron interactions are large on the energy scale of the expected narrow band width. We report angle-resolved photoemission data on the band dispersion for an alkali-doped C_{60} monolayer and a detailed comparison with theory. Compared to the maximum bare theoretical band width of 170 meV, the observed 100-meV dispersion is within the range of renormalization by electron-phonon coupling. This dispersion is only a fraction of the integrated peak width, revealing the importance of many-body effects. Additionally, measurements on the Fermi surface indicate the robustness of the Luttinger theorem even for materials with strong interactions.

Exhibiting properties such as high transition temperature superconductivity (*1*) and antiferromagnetism (*2*), C_{60}-based fullerides are ideal model compounds for exploring key conceptual issues in strongly correlated physics (*3*). As in typical molecular systems, the bands formed through the overlap of the C_{60} molecular levels are expected to be narrow, on the order of 0.5 eV for the lowest unoccupied molecular orbital (LUMO)–derived band (*4*). On the other hand, the Coulomb repulsion between electrons is larger [more than 1 eV (*5*)], and some phonons have very high energies [up to 200 meV (*3*)] comparable to the expected bandwidth of half-filling. This set of parameters suggests a totally nonconventional behavior: On one hand, the strong electron-electron interaction predicts the proximity of metal-insulator transitions of the Mott-Hubbard type, whereas the high phonon frequencies predict a breakdown of the adiabatic approximation. In angle-integrated photoemission measurements (AIPES), the width of the LUMO peak, which naively corresponds to the band width, appears much wider (~1 eV) than the theo-

retical estimation. Although of fundamental importance to addressing this issue, the observation of band dispersion has remained elusive after a decade of intense efforts. This is a testimony to the technical challenges imposed by the detection of such a narrow band, with threefold degeneracy, in a small Brillouin zone (BZ), as well as particular matrix element effects and/or disorder in samples. We detected with synchrotron light a clear band dispersion of 100 meV for a C_{60} monolayer doped by K to approximately half-filling, indicating that the width of the AIPES measurement is mainly because of many-body effects. The experimental results are compared with a theoretical calculation performed for the same monolayer system. Both the band width and Fermi velocity are renormalized by 40 to 50% as compared with the maximum bare theoretical dispersion of 170 meV and the calculated Fermi velocity. This upper bound of renormalization is within the range explainable by electron-phonon coupling alone using values of the electron-phonon coupling constant from the literature (*3*). This suggests that the electron-electron correlation is not substantial in reducing the bandwidth in our monolayers although it is expected to be strong in this system (*3*, *5*). An extremely short mean-free path can be inferred from the momentum peak width but does not preclude a complete mapping of the Fermi surface (FS). Its volume obeys the Luttinger theorem, although the complex interactions and short mean-free path may question its validity.

We carried out high-resolution angle-resolved photoelectron spectroscopy (ARPES) on single crystalline K-doped C_{60} monolayers prepared in situ. The ARPES data presented here were collected with photon energy of 35 eV and with the direction of incident beam polarization almost perpendicular to the sample surface, whereas results have been confirmed with the use of other photon energies and on different samples (*6*).

A thick multilayer C_{60} film, grown at 400 K, was annealed at above 600 K to yield a C_{60} monolayer (*7*–*9*). K was then introduced with the use of an SAES getter source [for example, (*7*, *10*)]. The low-energy electron diffraction (LEED) patterns (Fig. 1, A to C) indicate a hexagonal lattice structure of C_{60} monolayer (Fig. 1, B and C) on the Ag(111) surface (Fig. 1A). The distance between C_{60}

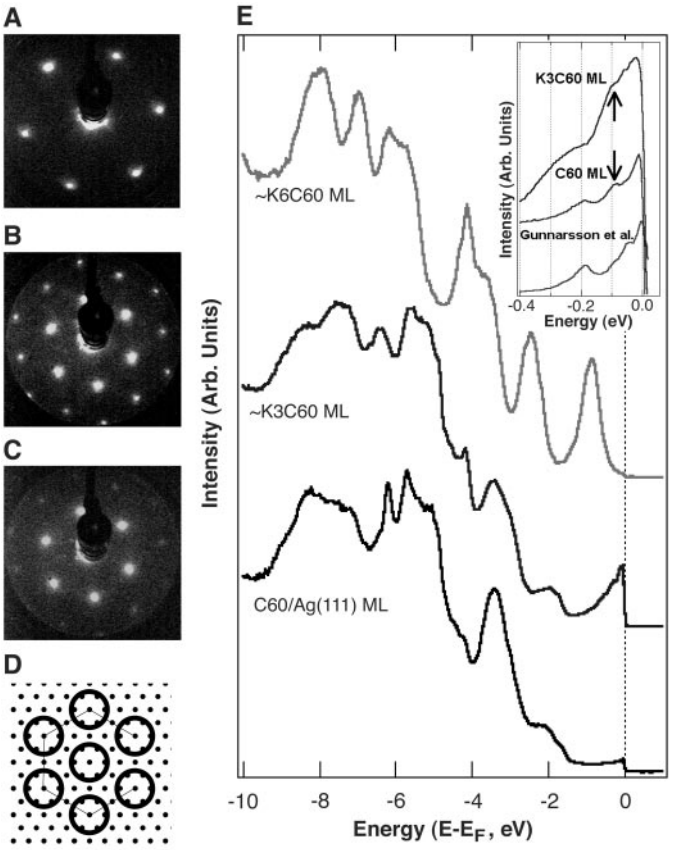

Fig. 1. LEED patterns and angle-integrated photoemission data. LEED patterns of (**A**) a clean Ag(111) surface at 114 eV electron beam energy, (**B**) a pure C_{60} monolayer at 22 eV, and (**C**) a K_3C_{60} monolayer at 22 eV. The orientation of the hexagon in (B) and (C) is rotated by 30° compared to (A). (**D**) Schematic view of the real space structure of C_{60} molecules (larger circles) on Ag(111) surfaces (small dots). (**E**) Valence band measured by angle-integrated photoemission on C_{60}, K_3C_{60}, and K_6C_{60} monolayers (MLs). The inset is an enlargement of the spectra near Fermi level as compared to data digitized from (*12*).

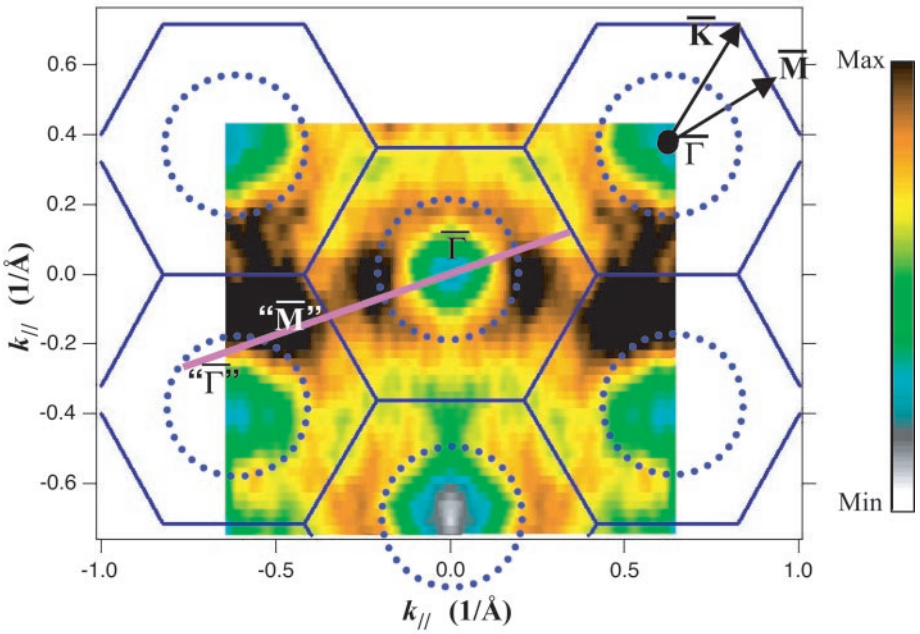

Fig. 2. Integrated spectral weight near the Fermi energy on K_3C_{60} monolayer. BZ boundaries (straight lines) are calculated on the basis of LEED. Dotted circles are guides showing a ring-like shape surrounding each $\bar{\Gamma}$ point. The occupied states are along zone boundaries. The data were taken in the left half of the color image and were symmetrized along the $x = 0$ line accordingly with symmetry consideration. The purple line shows the measuring direction for the dispersion in Fig. 3. $k_{//}$ is the electron momentum, and the color scale indicates the minimum and maximum of the intensity.

[1]Advanced Light Source (ALS), [2]Materials Science Division, Lawrence Berkeley National Laboratory (LBNL), Berkeley, CA 94720, USA. [3]Department of Physics, Department of Applied Physics, and Stanford Synchrotron Radiation Laboratory (SSRL), Stanford University, Stanford, CA 94305, USA. [4]Laboratoire de Physique des Solides, CNRS, UMR8502, Universite Paris-Sud, Bat 510, 91405 Orsay, France. [5]Department of Physics, University of California at Berkeley, Berkeley, CA 94720, USA. [6]Sincrotrone Trieste S.C.p.A., S.S. 14 Km 163.5, in Area Science Park, 34012 Trieste, Italy. [7]Istituto Nazionale per la Fisica della Materia–Dipartimento di Matematica e Fisica, Università Cattolica del Sacro Cuore, Via dei Musei 41, 25121 Brescia, Italy.

*To whom correspondence should be addressed. E-mail: zxshen@stanford.edu

molecules is estimated to be 10.02 Å from the Ag fcc lattice constant (Fig. 1D).

Figure 1E depicts three AIPES data measured on C_{60} films with and without K doping. For the pure C_{60} monolayer, there is a small contribution to the density of states at the Fermi level because of the charge transfer from the Ag substrate. With K doping, the LUMO-derived band, which is triply degenerated (*4*), is filled by electrons from K up to K_6C_{60} (*7*, *11*). By integrating the LUMO peaks in AIPES data and taking the K_6C_{60} spectra as a reference with charge transfer of 6 (Fig. 1E), we estimated the charge transfer to C_{60} molecules to be about 0.7 for the pure C_{60} monolayer [comparable to 0.75 in (*7*)], and 3.3 for the intermediately K-doped sample, which we refer to as a K_3C_{60} monolayer hereafter. The peak at the Fermi level, together with the shoulders at higher energy (Fig. 1E, inset), resemble those observed in the gas-phase C_{60}^-, where the shoulders were interpreted in terms of phonon satellites (*12*, *13*). This feature is clearer in the pure C_{60} monolayer compared to K-doped samples. The 100-meV phonon behavior is enhanced compared with the gas-phase data, suggesting a modification due to band structure effect and/or electron-phonon coupling.

The two-dimensional (2D) FS map of the K_3C_{60} monolayer (Fig. 2) shows a periodicity in momentum space that matches very well with the C_{60} BZ deduced from LEED. This map, obtained by integrating the spectral weight over a ±20-meV energy window at the Fermi level throughout the BZ, shows a ring encircling low spectral intensity around each $\bar{\Gamma}$ point for all the BZs. As discussed below, these low-intensity regions are unoccupied states, so we have a hole-like circular 2D FS around each $\bar{\Gamma}$. The change of the intensity at the equivalent symmetric points may be because of matrix element effect and/or asymmetries from measuring geometry. A similar result was also verified with the use of 45-eV photons.

The dispersion of the partially filled conduction (LUMO-derived) band was determined, approximately along the $\bar{\Gamma}$-$\bar{M}$ direction (purple line in Fig. 2), from angle-resolved EDCs (energy distribution curves). The band disperses in the energy scale of about 100 meV and crosses the Fermi level at 0.15 to 0.2 $Å^{-1}$ in momentum space (Fig. 3, A to C). This result shows that the closed area around the $\bar{\Gamma}$ point is "unoccupied," and the occupied states are along the BZ boundary, complementing the results of the FS map (Fig. 2). To extract the shape of the dispersion quantitatively near the Fermi level, we studied the MDCs (momentum distribution curves), and the positions of the MDC peaks around Fermi level are shown as the purple dots in Fig. 3B. The Fermi velocity, v_F, defined as the slope of the dispersion at Fermi energy (E_F), is 7.9 (±0.9) × 10^6 cm s^{-1}, corresponding to an effective mass of m^* equal to $2m_e$ to $4m_e$ (m_e is the free electron mass).

For quantitative analysis, we studied the crystal and electronic structures of K_3C_{60} monolayers with the use of ab initio pseudopotential density functional calculations (*14*–*17*) in the local density approximation (LDA). The positions of the three K atoms and the center of mass of the C_{60} molecule are relaxed according to ab initio forces on top of the Ag surface represented by six layers of Ag atoms. The calculated LUMO-derived band dispersions are so sensitive to the orientations of C_{60} molecules that we can determine a very specific orientation of C_{60} as a model for the experimental samples by comparing the theoretical disper-

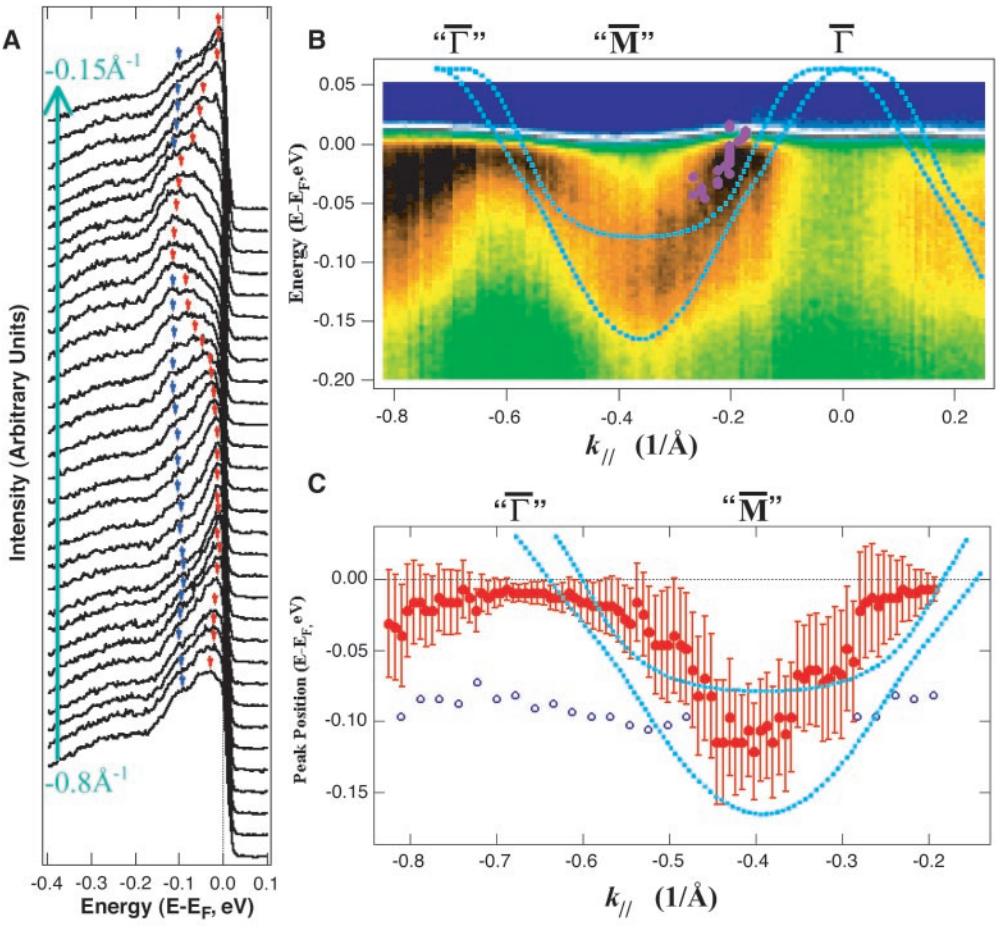

Fig. 3. Band dispersion measured on a K_3C_{60} monolayer at 35 eV photon energy. The measuring direction, which is approximately along $\bar{\Gamma}$-$\bar{M}$, is indicated by the purple line in Fig. 2. (**A**) Angle-resolved EDCs with emission angle from −0.8 $Å^{-1}$ (–16.5°) to −0.15 $Å^{-1}$ (–3°). The red arrows show the main peak position, also plotted in (C) as the red solid circles, corresponding to the band dispersion. The weak peak at 100 meV (blue arrows), also shown as the blue circle in (C), is probably because of phonon shake-up structure. (**B**) Image plot of photoelectron intensity versus energy and emission angle. Data were collected on two samples below and above $x = -0.2$ $Å^{-1}$, respectively, with very good reproducibility. Color legend is the same as that of Fig. 2. The band disperses above Fermi level around each $\bar{\Gamma}$ point. For comparison, two subbands from theoretical calculations are shown as dotted lines. At the second BZ, the intensity below Fermi level around "$\bar{\Gamma}$" is probably because of the misalignment (about 12° off the $\bar{\Gamma}$-$\bar{M}$ direction as shown in Fig. 2), which may also mix some contribution of the $\bar{\Gamma}$-$\bar{\Gamma}$ component. This misalignment also contributes to the a-little-shorter experimental $\bar{\Gamma}$-"$\bar{\Gamma}$" distance as compared to theory. The extremely narrow band and small BZ make high zone measurements more difficult. (**C**) The maximum peak position of EDCs in (A) (red solid circles). The error bars correspond to the peak widths in (A). The dotted lines are again the calculated bands, which are shifted left by 0.03 $Å^{-1}$ (0.6° in emission angle, within experimental error bar) to match the experimental data better. We cannot resolve the two subbands in our experiments, but the maximum experimental dispersion (100 meV) is smaller than that of the theoretical one (170 meV). This gives an upper bound of renormalization, although it can be smaller if one takes some sort of average of the theoretical bands.

sions with the experiments. The obtained model orientation (Fig. 4A), whose total energy is only 0.1 eV per C_{60} higher than the minimum, is very close to that in solid K_3C_{60}. Because the energy difference is so small ($\sim 1 \times 10^{-3}$ rydberg per atom), it is well within the uncertainties of the LDA for van der Waals solids.

The calculated LUMO-derived bands (Fig. 4B) are not occupied around the $\bar{\Gamma}$ point, consistent with experimental data (Fig. 3B). The maximum width of the occupied band is 170 meV, and the Fermi velocities are 1.2×10^7 and 1.6×10^7 cm s^{-1} for two LUMO-derived subbands, respectively. Both the band width and the Fermi velocity overestimate the experimental results by 40 to 50%, implying that the renormalization of the band width and Fermi velocity from many-body effects is about a factor of 2 or smaller. Considering the electron-phonon coupling constant $\lambda = 1$ (*12*), the renormalization is within the range explainable by electron-phonon coupling alone ($1 + \lambda = 2$). Therefore, the expected strong electron-electron correlation in the system (*5*) does not cause a substantial reduction of the band width, consistent with the density of states extracted from specific heat measurements in bulk A_3C_{60} [(*18*) and the discussions in (*19*)]. Alternatively, the Coulomb interaction on C_{60} molecules could be suppressed because of the screening effect from the metal substrates in our monolayer samples (*20*).

From the volume of FS, we can estimate the amount of charge transfer by assuming that the observed experimental dispersion (Fig. 3B) corresponds to two unresolved bands (Fig. 4B). The unoccupied area around a $\bar{\Gamma}$ point in the 2D FS map (Fig. 2) is about 15 to 40% of the volume of a BZ. Therefore, the charge transfer is [1–(15 to 40%)] × 2 (charged subbands) × 2 (electrons per band) ≈ 2.9 (±0.5) electrons, consistent with 3.3 deduced from the AIPES intensity (Fig. 1E). Although the integral method for determining the charge transfer may have some error (*11*), this rough analysis suggests that the Luttinger theorem is valid in our electron-doped C_{60} systems.

The clear observation of electronic band structures and Luttinger Fermi surface in K-doped C_{60} is remarkable when considering the very short mean-free path estimated in this system (*21*). The peak width at E_F extracted from MDC is $\Delta k = 0.14 \pm 0.02$ Å^{-1}, yielding a mean-free path $l = 1/\Delta k = 7.4 \pm 0.9$ Å here at the experimental temperature, about 25 K. This value is smaller than the nearest-neighbor distance between C_{60} molecules (~10 Å) but larger than the shortest C-C distance between two adjacent molecules (~3 Å). It is still unexpected that we can see very clear dispersion and the Luttinger Fermi surface given such a short l.

Our data show that photoemission data for the C_{60} family consist of a coherent part near Fermi level and an incoherent part below ~100 meV (*22*). The much larger value of AIPES peak width, 700 to 1200 meV (Fig. 1) (*7*, *11*, *23*, *24*), is mainly due to many-body effects (*25*). The coherent band shows dispersing peaks and Fermi surface, and the incoherent features are characterized by a peak at 100 meV and a broad shoulder at about 250 meV (Fig. 1E) (*23*). The weak 100-meV peak shows very little dispersion (small blue arrows in Fig. 3A and blue circles in Fig. 3C), and its energy position is nearly doping-independent (Fig. 1E, inset). This can be attributed to phonons, as also discussed above with AIPES data. We do know that there are two phonon modes near this energy in the C_{60} system (*3*), but the coupling with them would have to be stronger to give rise to a sharper peak than that with other modes. One possibility is that these phonons could yield a special feature in the self-energy, because their frequency is comparable to the bandwidth, which is an unusual situation but typical of fullerides. In such a case, the spectral weight may be pushed beyond the band edge (*26*), leading to the formation of the 100-meV peak and/or part of the 250-meV shoulder. This 250-meV shoulder might also be attributed to high electron-electron correlation in analogy to the remnant of lower Hubbard band (*23*).

The data presented here indicate that the C_{60} system resembles the cuprates or other transition-metal oxides in many ways. In both cases, despite the strong interactions, the effective mass of the "quasi-particle band" is only slightly renormalized, and the velocity of the quasi-particle remains high. In both cases, Fermi surfaces with about the correct Luttinger volume are observed in spite of the extremely short mean-free path, and even the systems have a strong tendency to show inhomogeneity at a very small length scale. This suggests that the Fermi surface and dispersion carry more information on local bonding. It would be very interesting to see whether one can extract more quantitative information by comparing the present data with theoretical calculations such as those using the dynamic mean-field theory (*27*, *28*), which also starts from a local perspective.

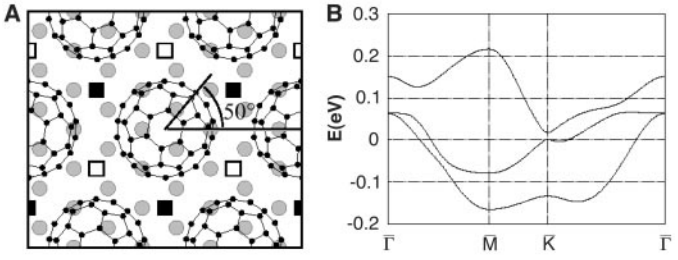

Fig. 4. Theoretical band dispersion of a K_3C_{60} monolayer. (**A**) Atomic configuration of a K_3C_{60} monolayer that results in the best agreement between the theoretical and the experimental band dispersions. Black dots represent C atoms in the upper half of the molecules, and gray dots represent Ag atoms of the top layer of the Ag(111) surface. A threefold axis of C_{60} is normal to the surface, and a center of a pentagon close to the axis has an angle of 50° with respect to a nearest-neighbor direction. The center of C_{60} is 5.6 Å away from the Ag surface. One K atom is located at each open square (3.5 Å away from the Ag surface), and two K atoms are at each solid square (2.9 and 7.6 Å away, respectively). With an angle of 53°, the positions of the C atoms would be the same as those in a (111) layer of solid K_3C_{60}. (**B**) Theoretical band dispersion of a K_3C_{60} monolayer with the orientational configuration of (A). The Fermi level is set to zero in the plot.

References and Notes

1. A. F. Hebard *et al.*, *Nature* **350**, 600 (1991).
2. T. Takenobu, T. Muro, Y. Iwasa, T. Mitani, *Phys. Rev. Lett.* **85**, 381 (2000).
3. O. Gunnarsson, *Rev. Mod. Phys.* **69**, 575 (1997).
4. S. C. Erwin, W. E. Pickett, *Science* **254**, 842 (1991).
5. R. W. Lof, M. A. Veenendaal, B. Koopmans, H. T. Jonkman, G. A. Sawatzky, *Phys. Rev. Lett.* **68**, 3924 (1992).
6. ARPES data were collected at the undulator beamline 10.0.1 of the ALS with a linearly polarized synchrotron beam and tunable photon energy and the use of angular mode I of the Scienta 2002 analyzer. AIPES data were collected with the use of the transmission mode. The energy resolution for ARPES experiments reported here is 10 to 15 meV, and the angular resolution for mode I is ±0.15° along the analyzer slit and ±0.25° in the perpendicular direction. (Angular mode II gives a better resolution of ±0.05° along the slit, but mode I was used for this work to get sufficient statictics.) The 127 individual spectra along the ~13° slit could be collected simultaneously. A detailed description is also available in some recent publications, e.g., (*29*–*31*). LEED patterns were collected with the use of Er-LEED from Specs (Berlin, Germany).
7. L. H. Tjeng *et al.*, *Solid State Commun.* **103**, 31 (1997).
8. E. I. Altman, R. J. Colton, *Phys. Rev. B* **48**, 18244 (1993).
9. S. Modesti, S. Cerasari, P. Rudolf, *Phys. Rev. Lett.* **71**, 2469 (1993).
10. B. W. Hoogenboom, R. Hesper, L. H. Tjeng, G. A. Sawatzky, *Phys. Rev. B* **57**, 11939 (1998).
11. C. Cepek, M. Sancrotti, T. Greber, J. Osterwalder, *Surf. Sci.* **454–456**, 467 (2000).
12. O. Gunnarsson *et al.*, *Phys. Rev. Lett.* **74**, 1875 (1995).
13. M. Knupfer, M. Merkel, M. S. Golden, J. Fink, *Phys. Rev. B* **47**, 13944 (1993).
14. M. L. Cohen, *Phys. Scr.* **T1**, 5 (1982).
15. N. Troullier, J. L. Martins, *Phys. Rev. B* **43**, 1993 (1991).
16. J. Ihm, A. Zunger, M. L. Cohen, *J. Phys. Solid State Phys.* **12**, 4409 (1979).
17. D. Sánchez-Portal, P. Ordejón, E. Artacho, J. M. Soler, *Int. J. Quantum Chem.* **65**, 453 (1997).
18. G. J. Burkhart, C. Meingast, *Phys. Rev. B* **54**, R6865 (1996).
19. F. Aryasetiawan, O. Gunnarsson, E. Koch, R. M. Martin, *Phys. Rev. B* **55**, R10165 (1997).
20. R. Hesper, L. H. Tjeng, G. A. Sawatzky, *Europhys. Lett.* **40**(2), 177 (1997).
21. A. F. Hebard, T. T. M. Palstra, R. C. Haddon, R. M. Fleming, *Phys. Rev. B* **48**, 9945 (1993).

22. A. Goldoni *et al.*, *J. Chem. Phys.* **113**, 8266 (2000).
23. P. J. Benning *et al.*, *Phys. Rev. B* **47**, 13843 (1993).
24. R. Hesper, L. H. Tjeng, A. Heeres, G. A. Sawatzky, *Phys. Rev. B* **62**, 16046 (2000).
25. V. P. Antropov, O. Gunnarsson, A. I. Liechtenstein, *Phys. Rev. B* **48**, 7651 (1993).
26. A. I. Liechtenstein, O. Gunnarsson, M. Knupfer, J. Fink, J. F. Armbruster, *J. Phys. Condens. Matter* **8**, 4001 (1996).
27. A. Georges, G. Kotliar, W. Krauth, M. J. Rozenberg, *Rev. Mod. Phys.* **68**, 13 (1996).
28. M. Capone, M. Fabrizio, C. Castellani, E. Tosatti, *Science* **296**, 2364 (2002).
29. X. J. Zhou *et al.*, *Science* **286**, 268 (1999).
30. Y.-D. Chuang, A. D. Gromko, D. S. Dessau, T. Kimura, Y. Tokura, *Science* **292**, 1509 (2001); published online 26 April 2001 (10.1126/science.1059255).
31. P. V. Bogdanov *et al.*, *Phys. Rev. Lett.* **85**, 2581 (2000).
32. We thank O. Gunnarsson and J. Osterwalder for stimulating discussions. Y.W.L. is grateful to J. Pepper for excellent technical support. The experiments were performed at the ALS of LBNL, which is operated by the U.S. Department of Energy (DOE), Office of Basic Energy Sciences (BES), Division of Material Science, with contract DE-AC03-76SF00098. The division also provided support for the work at SSRL with contract DE-FG03-01ER45929-A001. The work at Stanford was supported by Office of Naval Research grant N00014-98-1-0195-P0007 and NSF grant DMR-0071897. The theoretical work was supported by NSF grant DMR-0087088 and the DOE's Office of BES under contract DE-AC03-76SF00098. Computational resources have been provided by NSF at the National Center for Supercomputing Applications and by the National Energy Research Scientific Computing Center.

8 January 2003; accepted 14 March 2003

Enhanced Upper Tropical Tropospheric COS: Impact on the Stratospheric Aerosol Layer

J. Notholt,[1]* Z. Kuang,[2]† C. P. Rinsland,[3] G. C. Toon,[4] M. Rex,[5] N. Jones,[6] T. Albrecht,[5] H. Deckelmann,[5] J. Krieg,[5] C. Weinzierl,[1] H. Bingemer,[7] R. Weller,[8] O. Schrems[8]

Carbonyl sulfide (COS) is considered to be a major source of the stratospheric sulfate aerosol during periods of volcanic quiescence. We measured COS at the tropical tropopause and find mixing ratios to be 20 to 50% larger than are assumed in models. The enhanced COS levels are correlated with high concentrations of biomass-burning pollutants like carbon monoxide (CO) and hydrogen cyanide (HCN). The analysis of backward trajectories and global maps of fire statistics suggest that biomass-burning emissions transported upward by deep convection are the source of the enhanced COS in the upper tropical troposphere.

The main sources of COS are direct emissions at the surface and the conversion of CS_2 and DMS (dimethylsulfide) in the atmosphere (*1*–*3*). Biomass burning is assumed to contribute 10 to 20% to the overall source strength of COS (*4*–*6*). Because of its long lifetime, the COS mixing ratio is relatively constant throughout the troposphere at about 500 parts per trillion by volume (pptv) (*1*, *7*, *8*), although a small decline of 0.25%/year throughout the past 24 years has been recorded (*9*). The available data on the vertical profiles of COS exhibit no significant vertical gradient in the troposphere and a slow decrease above the tropopause (*1*). Much of the COS reaches the stratosphere, where photolysis and oxidation lead to the production of SO_2 and eventually to sulfate particles (*2*, *4*, *10*). The stratospheric aerosol layer has an important impact on the radiation budget of the stratosphere, its dynamical structure, and its chemistry (*11*). With the exception of SO_2, other sulfur compounds, such as CS_2 or DMS, have much shorter lifetimes than COS and are assumed not to contribute appreciably to the sulfur budget in the stratosphere except during volcanic eruptions (*2*).

Here we present observations of COS and other related trace gases in the upper tropical tropopause region. The measurements were performed by passive absorption spectrometry in the infrared with the Sun as light source (*12*). We discuss ground-based observations performed during two Atlantic cruises on board the German research vessel *Polarstern*, where the tropics were passed in October to November 1996 and December to January 1999–2000. These observations are complemented by space-borne observations above the Pacific from the ATMOS instrument flown on board the space shuttle in November 1994.

Absorption spectra of COS and CO were analyzed in the spectral region between 2000 and 2200 cm^{-1}. The spectroscopic data for all molecules were taken from the most recent versions of the HITRAN and ATMOS database (*13*). The inversion of the cruise spectra to retrieve the trace-gas concentrations was implemented with SFIT2, an optimal estimation method, developed at NASA Langley and at the National Institute for Water and Atmospheric Research (NIWA) in Lauder, New Zealand (*9*). The pressure broadening of isolated spectral lines enables the determination of vertical concentration profiles up to a 30-km altitude, with relatively coarse resolution of ~4 km in the altitude region discussed here. The initial mixing ratios for all trace gases for the cruise analysis are based on balloon observations. For the cruise data, we estimate the precision of COS and CO to be on the order of 10 to 15% for averaged altitude layers of 4-km thickness (*14*). The ATMOS spectra were recorded in November 1994 during sunset in occultation geometry, yielding the concentration profiles with an altitude resolution of ~1 to 2 km (*15*). These spectra were analyzed with GFIT, a code developed for the analysis of balloon and satellite spectra (*16*). The error bars on the ATMOS volume mixing ratio (VMR) profiles represent their precision, which is estimated from the goodness of the fits to the measured spectra.

The cruise data from the Atlantic (Fig. 1) show an unexpected positive gradient of the mixing ratio of COS between the ground and the tropical tropopause during both cruises. Enhanced mixing ratios up to 600 pptv were found below the tropical tropopause, at altitudes between 10 and 18 km. The ship-borne observations are supported by the ATMOS observations from the tropical Pacific (Fig. 2), which also reveal a COS enhancement in the upper tropical troposphere at 16 km. Although the COS enhancement of the individual profile shown is within the order of the uncertainty, other ATMOS profiles close to the equator consistently show the same feature.

Numerous studies of the composition of the tropical troposphere, including observations of COS, were performed during several campaigns, e.g., PEM-West, PEM-Tropics, Safari, and Trace-A (*17*–*19*). However, these COS measurements were limited to altitudes below 12 km. The only previous COS measurements in the upper tropical troposphere were reported by Leifer (*20*).

[1]University of Bremen, D-28334 Bremen, Germany. [2]California Institute of Technology, Pasadena, CA 91125, USA. [3]NASA Langley Research Center, Hampton, VA 23681–2199, USA. [4]Jet Propulsion Laboratory, California Institute of Technology, Pasadena, CA 91109, USA. [5]Alfred Wegener Institute for Polar and Marine Research, D-14473 Potsdam, Germany. [6]University of Wollongong, Wollongong, New South Wales 2522, Australia. [7]J. W. Goethe–University, D-60325 Frankfurt am Main, Germany. [8]Alfred Wegener Institute for Polar and Marine Research, D-27568 Bremerhaven, Germany.

*To whom correspondence should be addressed. E-mail: jnotholt@iup.physik.uni-bremen.de
†Present address: University of Washington, Seattle, WA 98195–1640, USA.